

IS HESS J1912+101 ASSOCIATED WITH AN OLD SUPERNOVA REMNANT?

YANG SU,¹ XIN ZHOU,¹ JI YANG,¹ YANG CHEN,^{2,3} XUEPENG CHEN,¹ YAN GONG,¹ AND
 SHAOBO ZHANG¹

¹*Purple Mountain Observatory and Key Laboratory of Radio Astronomy, Chinese Academy of Sciences, Nanjing 210008, China*

²*Department of Astronomy, Nanjing University, Nanjing 210023, China*

³*Key Laboratory of Modern Astronomy and Astrophysics, Nanjing University, Ministry of Education, Nanjing 210023, China*

ABSTRACT

HESS J1912+101 is a shell-like TeV source that has no clear counterpart in multiwavelength. Using CO and H I data, we reveal that $V_{\text{LSR}} \sim +60 \text{ km s}^{-1}$ molecular clouds (MCs), together with shocked molecular gas and high-velocity neutral atomic shells, are concentrated toward HESS J1912+101. The prominent wing profiles up to $V_{\text{LSR}} \sim +80 \text{ km s}^{-1}$ seen in ^{12}CO ($J=1-0$ and $J=3-2$) data, as well as the high-velocity expanding H I shells up to $V_{\text{LSR}} \sim +100 \text{ km s}^{-1}$, exhibit striking redshifted-broadening relative to the quiescent gas. These features provide compelling evidences for large-scale perturbation in the region. We argue that the shocked MCs and the high-velocity H I shells may originate from an old supernova remnant (SNR). The distance to the SNR is estimated to be $\sim 4.1 \text{ kpc}$ based on the H I self-absorption method, which leads to a physical radius of 29.0 pc for the $\sim (0.7-2.0) \times 10^5$ years old remnant with an expansion velocity of $\gtrsim 40 \text{ km s}^{-1}$. The $+60 \text{ km s}^{-1}$ MCs and the disturbed gas are indeed found to coincide with the bright TeV emission, supporting the physical association between them. Naturally, the shell-like TeV emission comes from the decay of neutral pions produced by interactions between the accelerated hadrons from the SNR and the surrounding high-density molecular gas.

Keywords: ISM: individual objects (shell-like clouds, HESS J1912+101) – ISM: kinematics and dynamics – ISM: supernova remnants

1. INTRODUCTION

Shell-type supernova remnants (SNRs) are believed to be efficient accelerators of high-energy cosmic rays (CRs) through diffusive shock acceleration (e.g., see the recent review of Reynolds 2008). Such strong shocks of young SNRs put considerable energy into accelerated particles of CRs, resulting in high-energy X-ray and γ -ray emission. On the other hand, pp-interactions and the subsequent decay of neutral pions will significantly enhance the γ -ray emission in high-density environments. Molecular clouds (MCs) near SNRs are thus promising sources of γ -ray emission because of their high densities. Recently, theoretical (e.g., Yamazaki et al. 2006; Fujita et al. 2009; Li & Chen 2010; Ohira et al. 2011) and observational studies (e.g., Aharonian et al. 2008aa; Tian et al. 2008; Castro & Slane 2010; Tavani et al. 2010; Ackermann et al. 2013) have been performed to investigate the high-energy γ -ray emission toward SNRs and their ambient molecular gas (e.g., see a summary in Slane et al. 2015).

HESS J1912+101 is an extended TeV source that was discovered by Aharonian et al. (2008b) and displays the prominent shell appearance of the TeV emission from the further increased H.E.S.S. exposure (Puehlhofer et al. 2015). However, no firm conclusion on the nature of the source can be drawn, due to the lack of the counterpart of HESS J1912+101 at other wavebands. The TeV source was speculated to associate with a high spin-down luminosity pulsar PSR J1913+1011 or an old SNR (Aharonian et al. 2008b). The pulsar wind nebulae (PWN) scenario may be excluded because of no detectable X-ray emission around PSR J1913+1011 and/or the geometrical centroid of HESS J1912+101 (Chang et al. 2008) and the presence of the TeV shell-like structure. Therefore, the shell-like source of HESS J1912+101 is probably a TeV SNR candidate (Puehlhofer et al. 2015; Gottschall et al. 2016), although no corresponding radio counterpart has been found to match the TeV shell structure yet.

The high angular resolution of the very-high-energy (VHE, $E > 100$ GeV) data, which is better than $0''.1$ for the H.E.S.S. observation, allows us to compare the TeV structure with that seen in other wavelengths with the precision of several arcmin. Because little corresponding radio and X-ray emission matches the high-energy source, typical structures of the molecular and/or atomic gas on a large scale (e.g., shells, arcs, and bubbles, etc.), together with possible kinematic signatures of the disturbed gas (e.g., molecular line broadenings, high-velocity structures, and large-velocity gradients, etc.), are useful and important in investigating the association between HESS J1912+101 and its environment.

In this paper, we present the molecular and atomic line study toward the shell-like TeV source of HESS J1912+101. Both of CO and HI datasets reveal the partial shell-like structures and high-velocity gas emission in the field of view (FOV) of the TeV source, indicating an energetic source with high momentum and mechanical energy injection there. We suggest that the energetic source is an old SNR that is interacting with the surrounding $V_{\text{LSR}} \sim +60$ km s $^{-1}$ giant MC (GMC) located at a near kinematic distance of 4.1 kpc. Accordingly, the shell-like TeV γ -ray emission of HESS J1912+101 arises from the interaction between the $(0.7\text{--}2.0) \times 10^5$ years old SNR and its ambient dense molecular gas.

This paper is structured as follows. In Section 2, we briefly describe the CO observation, the data reduction, and other survey data used in the paper. In Section 3, we give our results of the shocked molecular gas and the high-velocity HI shells; investigate the association between the disturbed gas and an old SNR; and discuss the origin of the shell-like TeV emission of HESS J1912+101. Finally, Section 4 summarizes the results.

2. CO AND HI DATA

CO datasets are from the Milky Way Imaging Scroll Painting (MWISP¹, i.e., ^{12}CO ($J=1-0$), ^{13}CO ($J=1-0$), and C^{18}O ($J=1-0$) lines) and CO High-Resolution Survey (COHRS, ^{12}CO ($J=3-2$) line; Dempsey et al. 2013). The HI and 21 cm continuum emission data are from the VLA Galactic Plane Survey (VGPS; Stil et al. 2006).

The MWISP project is a large, unbiased, and highly sensitive CO, and its isotopes survey toward the Galactic plane using the 13.7 m millimeter-wavelength telescope located at Delingha, China. A Superconducting Spectroscopic Array Receiver (SSAR) system with a 3×3 beam array (Shan et al. 2012) was used as the front end and a Fast Fourier Transform Spectrometer (FFTS) with a total bandwidth of 1 GHz was used as the back end. The half-power beamwidth (HPBW) of the telescope is about $50''$ for the three lines. The typical rms noise level is about 0.5 K for ^{12}CO ($J=1-0$) at the channel width of 0.16 km s^{-1} and 0.3 K for ^{13}CO ($J=1-0$) and C^{18}O ($J=1-0$) at 0.17 km s^{-1} . The final cube data were constructed with a grid spacing of $30''$. All data were reduced using the GILDAS software².

The information of the 13.7 m telescope can be seen from the status report³. The detailed observing strategy, the instrument, and the quality of the CO observations can be found in our paper published recently (see Section 2 in Su et al. 2017). We summarize the data used in Table 1.

3. RESULTS AND DISCUSSIONS

3.1. CO emission and the shocked molecular gas

HESS J1912+101 is a shell-like TeV source that is centered at ($l = 44^\circ 46'$, $b = -0^\circ 13'$) with an outer radius of $0^\circ 49'$ and an inner radius of $0^\circ 32'$ (Gottschall et al. 2016). Neither radio nor X-ray emission was detected toward the shell-like TeV source. Due to the significant extinction in the direction of the inner Galactic plane, optical observations are difficult to establish the nature of the source. Therefore, the submillimeter, millimeter, and centimeter emission is probably helpful in studying the nature of the counterpart of HESS J1912+101.

Using the high-quality CO data, we find that molecular gas at a systemic velocity of $V_{\text{LSR}} \sim +60 \text{ km s}^{-1}$ is concentrated toward the extended emission of the TeV source. Generally, ^{12}CO emission, which is widely distributed in the FOV, is more diffuse and extended than that of ^{13}CO . After carefully checking the CO data channel by channel, we distinguish several molecular partial shell-like structures toward the TeV source of HESS J1912+101. These partial shells are relatively prominent in ^{13}CO emission, which exhibits distinct velocity-coherent structure over the long curved line (length $\gtrsim 10'$ and width $\lesssim 2'$; see the thick-dashed gold lines in Figure 2). Meanwhile, optically thin C^{18}O emission is also detected in some regions of partial shells, indicating the high-density there due to its rarer abundance.

Figure 1 shows the three-color intensity image of CO emission (^{12}CO in blue, ^{13}CO in green, and C^{18}O in red; $V_{\text{LSR}}=58.5\text{--}62.0 \text{ km s}^{-1}$) toward the TeV source. Assuming the ^{13}CO abundance of $N(\text{H}_2)/N(^{13}\text{CO}) \approx 7 \times 10^5$ (Frerking et al. 1982) and the C^{18}O abundance of $N(\text{H}_2)/N(\text{C}^{18}\text{O}) \approx 7 \times 10^6$ (Castets & Langer 1995), the H_2 number density of the dense part of the molecular shells traced by the optically thin ^{13}CO emission (denoted by the thick-dashed gold lines in Figure 2) is

¹ <http://english.dlh.pmo.cas.cn/ic/>

² <http://ascl.net/1305.010> or <http://www.iram.fr/IRAMFR/GILDAS>

³ <http://www.radioast.nsd.cn/mwisp.php>

$\sim 400\text{--}1600\text{ cm}^{-3}$ at a distance of 4.1 kpc (see Section 3.3) with the shell's width of $\sim 2'$. Adopting the mean CO-to-H₂ mass conversion factor $X_{\text{CO}} = 2 \times 10^{20}\text{ cm}^{-2}\text{K}^{-1}\text{km}^{-1}\text{s}$ (Bolatto et al. 2013), the total mass of the molecular partial shells traced by the optically thick ^{12}CO emission is about several thousands solar mass at a distance of 4.1 kpc. The total mass estimated from ^{13}CO and C^{18}O emission is somewhat less than that from ^{12}CO emission. The mean volume density of the $V_{\text{LSR}} = +60\text{ km s}^{-1}$ MCs is approximately several hundreds per cm^3 , while the density in some dense regions should be $> 10^3\text{ cm}^{-3}$.

Furthermore, in combination with the MWISP and COHRS data, we identify several shocked regions projected toward the interior of the TeV shell of HESS J1912+101 (see the four white circles of SC1–SC4 in Figure 1). By comparing the broadened ^{12}CO ($J=1\text{--}0$ and $3\text{--}2$) lines with the narrow ^{13}CO line, we can illustrate that the molecular gas in some regions exhibits striking redshifted-broadening with respect to the ambient MCs at $V_{\text{LSR}} \sim +60\text{ km s}^{-1}$. As shown in Figures 2, the broadened red wing of ^{12}CO ($J=3\text{--}2$) emission is obviously up to $V_{\text{LSR}} \sim +80\text{ km s}^{-1}$ from position–velocity (PV) diagrams of SC2 and SC4. The typical spectra of the four regions, which display prominent redshifted-broadenings in ^{12}CO ($J=1\text{--}0$ and $3\text{--}2$) emission, are shown in Figure 3.

Broadened profiles of ^{12}CO emission usually come from the turbulent molecular gas that is readily and significantly influenced by local shocks. On the contrary, the optically thin ^{13}CO emission is mainly from the quiescent and unperturbed MCs. Therefore, such features like broadenings, wings, or asymmetries in ^{12}CO spectra with respect to ^{13}CO line show convincing evidence for shocked and disrupted molecular material, which often occurs in SNR–MC interacting systems (e.g., Frail & Mitchell 1998; Reach et al. 2005; Jiang et al. 2010; Kilpatrick et al. 2016).

SC2, which is likely a part of the shocked broad molecular line (BML) shell (see the red contours near the arrow of PVSC2 in Figure 2), exhibits the association between the shocked medium at $V_{\text{LSR}} = 65\text{--}80\text{ km s}^{-1}$ from the ^{12}CO ($J=1\text{--}0$ and $3\text{--}2$) emission and the surrounding quiescent MCs at $V_{\text{LSR}} = +59.6\text{ km s}^{-1}$ from the ^{13}CO emission (see Figure 2). A piece of shocked gas or SC4 identified from broadened ^{12}CO ($J=3\text{--}2$) emission ($2'.0 \times 0'.5$, see the red contours near the arrow of PVSC4 in Figure 2) also displays the spatial coincidence with the nearby ^{13}CO partial shell structure at the peak velocity of $V_{\text{LSR}} = +60.3\text{ km s}^{-1}$. We make a PV diagram perpendicular to the main axis of SC4 in Figure 2, in which the BML region of SC4 (the red contours) is distinct from the quiescent gas traced by ^{13}CO emission (the blue contours). Especially, the shocked molecular gas shells traced by ^{12}CO ($J=3\text{--}2$) emission (the red contours in Figure 2) seem to resemble the unperturbed molecular shells traced by ^{13}CO emission (the thick-dashed gold lines in Figure 2). These features imply that the shocked gas is indeed physically associated with the quiescent MCs at $V_{\text{LSR}} \sim +60\text{ km s}^{-1}$.

We try to investigate the distribution of the shocked gas in the whole region of HESS J1912+101. However, the ^{12}CO ($J=1\text{--}0$) line profile may be contaminated by unrelated MCs along the same line of sight (LOS) in the direction of the inner Milky Way. Observations in higher CO transitions might show less confusion because the broadline emission in high J is relatively strong with respect to the quiescent MCs. Unfortunately, the whole region of HESS J1912+101 is not completely covered by the COHRS ^{12}CO ($J=3\text{--}2$) survey in the direction (see Table 1).

We attempt to construct a map of $I(^{12}\text{CO}, v1 : v2) - I(^{13}\text{CO}, v1 : v2) \times 7$ to illustrate the possible distribution of the shocked material, where $I(^{12}\text{CO}, v1 : v2)$ and $I(^{13}\text{CO}, v1 : v2)$ are the integrated intensity of ^{12}CO ($J=1\text{--}0$) and ^{13}CO ($J=1\text{--}0$) in the velocity range of $v1$ to $v2$, respectively. Here, we adopt $v1 = +67\text{ km s}^{-1}$ and $v2 = +75\text{ km s}^{-1}$. It roughly represents the velocity range of the possible

redshifted CO wing component. The map will reveal the ^{12}CO ($J=1-0$) enhancement ($\gtrsim 6 \text{ K km s}^{-1}$) in the velocity range of $67-75 \text{ km s}^{-1}$, which may sketch the distribution of the shocked gas after subtracting the contribution of the unrelated CO emission (controlled by $I(^{13}\text{CO}, v1 : v2) \times 7$) in the whole FOV toward HESS J1912+101.

The aim of the above operation is to reveal the potential redshifted-BML regions based on the ^{12}CO and ^{13}CO ($J=1-0$) lines. Generally, the emission of typical MCs is optically thick for ^{12}CO line and optically thin for ^{13}CO line. On the contrary, the shocked molecular gas will exhibit optically thin ^{12}CO emission with little ^{13}CO emission for the broadened wing component. Using $I(^{12}\text{CO}, 67:75) - I(^{13}\text{CO}, 67:75) \times 7$, we can filter out much of the molecular emission from the unrelated MCs in $67-75 \text{ km s}^{-1}$, leaving the enhanced ^{12}CO emission in the same velocity interval along the LOS. The revealed ^{12}CO enhancement is probably related to the BML regions for shocked gas. The shortcoming is that some shocked features in the map are lost because of the confusion between the unrelated MCs and the shocked gas along the LOS (e.g., SC1). Some realistic BML regions cannot be identified either due to the weak emission of the broadened ^{12}CO wing and the high criterion of $\Delta I \gtrsim 6 \text{ K km s}^{-1}$ (e.g., SC3).

Figure 4 displays the distribution of the possible BML regions, in which the enhanced ^{12}CO ($J=1-0$) emission in $67-75 \text{ km s}^{-1}$ (the red contours) is overlaid with the ^{13}CO emission in the velocity interval of $58.5-62.0 \text{ km s}^{-1}$. An intriguing result is that most of the ^{12}CO ($J=1-0$) enhancements are concentrated within the TeV shell. We make two PV diagrams along Slice 1 and Slice 2 (see Figure 4) to search for possible kinematic features of the shocked gas further. In the PV diagrams (Figure 5), the redshifted protrusions of SCa–SCd in ^{12}CO ($J=1-0$) emission are actually discerned from the quiescent ^{13}CO emission, suggesting that the samples of SCb–SCe are likely BML regions. We note that shocked molecular gas at SC2 and SC4 from the previous ^{12}CO ($J=3-2$) analysis is coincident well with its nearby strong ^{12}CO ($J=1-0$) wing emission in the velocity range of $67-75 \text{ km s}^{-1}$. Moreover, the identification of the possible shocked BML region SCa at ($l=44^\circ 508$, $b = -0^\circ 108$) is also confirmed by its broadened ^{12}CO ($J=3-2$) emission up to $V_{\text{LSR}} \sim +77 \text{ km s}^{-1}$ (see the extracted spectrum in Figure 6), strengthening the validity of this method.

Some BML regions identified from the ^{12}CO ($J=3-2$) emission (e.g., SC1 and SC3) do not correspond to red contours, indicating the missing identification in Figure 4. Of course, some fragmental structures of red contours outside the TeV shell are not the BML region either. Additionally, H II regions of HRDS G044.528–0.234 (Anderson et al. 2011) and VLA G044.3103+00.0410 (Urquhart et al. 2009) are associated with the strong ^{12}CO ($J=1-0$) emission in $67-75 \text{ km s}^{-1}$ of SCf and SCg, respectively. All of these show the complexity for the $67-75 \text{ km s}^{-1}$ CO emission in the large-scale FOV. Therefore, the red contours in Figure 4 only roughly outline the distribution of the possible BML regions in the field (e.g., SCa–SCe).

Further observations and analysis are needed in order to identify the more reliable distribution of the shocked molecular gas in the whole region. As seen in Figure 6, the intensity ratio between ^{12}CO ($J=3-2$) emission and ^{12}CO ($J=1-0$) emission is high for BML regions in the velocity interval of $71.6-81.6 \text{ km s}^{-1}$ (or the redshifted-broadening part), which is consistent with the suggestion that an enhanced high-to-low ratio in CO line wings of MCs is a clear and useful indicator of shocked gas (e.g., Seta et al. 1998). High J observations of CO are thus helpful in providing the unambiguous, direct signature of the distribution of the shocked material in the whole region of the TeV source.

3.2. High-velocity H I gas

In the above section, we have shown that the emission of the shocked molecular gas, which exhibits significant redshifted-broadening relative to the ambient gas, is concentrated toward the shell-like TeV source of HESS J1912+101 (Figures 2, 4, and 6). The LSR velocity of the shocked molecular gas exceeds that of the tangent points in the direction ($l=44^\circ 5$, $v_{\text{tangent}} = +71 \text{ km s}^{-1}$). As a result, one can readily discern that the disturbed gas from the surrounding emission if its LSR velocity is higher enough than the tangent point's velocity. Accordingly, we wonder whether the possible high-velocity atomic gas can be discerned from the background emission in the FOV.

Although the H I emission displays a complex spatial morphology and is more diffuse than CO emission in the FOV, two features of the high-velocity atomic gas are actually revealed toward the concentration of the shocked molecular gas based on VGPS H I data (see the blue contours in Figure 2). The LSR velocity of the atomic gas is high enough so that such expanding features can be distinguished from the surrounding background emission at positive velocities of $97.5\text{--}111.5 \text{ km s}^{-1}$. The high-velocity atomic gas, which is observed projected close to the western edge of the TeV source, is spatially coincident with the surrounding molecular partial shell structures at $\sim +60 \text{ km s}^{-1}$ traced by ^{13}CO emission (see the thick-dashed gold lines in Figure 2).

The atomic gas emission displays partial shell structures from northeast to southwest (length $\gtrsim 20'$ and width $\sim 4'$; see the blue contours and the thick-dashed blue lines in Figure 2). The emission of the high-velocity atomic gas is very faint ($\lesssim 2\text{--}3 \text{ K}$), but the shell structures are distinct from the background emission in the integrated intensity map of $V_{\text{LSR}} = 97.5 - 111.5 \text{ km s}^{-1}$. The H I emission of the shell structures drops dramatically at $V_{\text{LSR}} \sim +100 \text{ km s}^{-1}$ and seems to disappear at $V_{\text{LSR}} \sim +110 \text{ km s}^{-1}$. We cannot discern any H I structures from the integrated map of $V_{\text{LSR}} \geq +112 \text{ km s}^{-1}$. At velocities $\sim 80\text{--}90 \text{ km s}^{-1}$, the brightness temperature of the H I shells is $\sim 10 \text{ K}$, but the shell features are only marginally discerned due to confusion from the close by diffuse background emission.

The high-velocity H I gas Shell-a seems to be situated slightly outside the $\sim +60 \text{ km s}^{-1}$ molecular shell (Figure 2). It is also interesting to note that the shocked molecular gas (red contours for ^{12}CO ($J=3\text{--}2$) emission), the quiescent molecular gas (gray image for ^{13}CO ($J=1\text{--}0$) emission), and the high-velocity atomic gas (blue contours for H I emission) are in contact with each other and seem to display an ordered arrangement from the inner side to the outer side (or from southeast to northwest), indicating that these shells are probably physically associated. The close morphological agreement between the shocked molecular gas and the high-velocity H I gas, together with the redshifted velocities of the disturbed gas with respect to the $+60 \text{ km s}^{-1}$ quiescent gas, indicates that the gas shells probably have the same origin (see discussions in Section 3.3).

We summarize the properties of the high-velocity H I shells in Table 2. It should be noted that the estimated column density in Table 2 should be regarded as lower limits since the disturbed atomic gas at low velocities (e.g., $60\text{--}100 \text{ km s}^{-1}$) may have relatively higher T_{mean} than our estimates of $\sim 1 \text{ K}$ at $+100 \text{ km s}^{-1}$. Accordingly, the total mass and kinetic energy of the disturbed neutral gas in the Shell-a and Shell-b should also be viewed as lower limits.

3.3. An old SNR: its distance, age, and progenitor

So far, about one fourth of SNRs are thought to be associated with MCs (refer to, e.g., Jiang et al. 2010; Chen et al. 2014). These SNR–MC systems often display broadenings, wings, or asymmetric profiles in the molecular line spectra. On the other hand, some systematic searches for H I shells associated with Galactic SNRs were performed (e.g., Koo & Heiles 1991; Koo et al. 2004). Sev-

eral expanding HI shells are also confirmed to be associated with the SNR's radio emission (e.g., [Park et al. 2013](#)).

These studies suggest that a significant fraction of the SNR's mechanical energy is stored in the ambient interstellar medium (ISM). Disturbed by the SNR shock, the material in the vicinity of the remnant will be swept up and exhibit expanding molecular and/or atomic shell-like structures on a large scale. These shell-like features are often incomplete because of the inhomogeneous ISM.

Both shocked molecular gas and the associated expanding HI shells are found to be physically associated with MCs at $V_{\text{LSR}} \sim +60 \text{ km s}^{-1}$ (see Sections 3.1 and 3.2). It is thus natural to ascribe the disturbed gas to the perturbation of an SNR in the region. In such a scenario, the SNR provides the required kinetic energy and momentum for its ambient disturbed material. Broadly speaking, HI gas, tracing emission of more diffuse gas, may be swept farther away than molecular gas if the interaction happens early enough. As seen in Figure 2, Gas Shell-a may be the expected case that the high-velocity atomic gas displays more redshifted velocity structure with respect to that of the shocked molecular gas and expands somewhat farther toward the northwestern direction than the associated CO shell.

The separation between the molecular shell and the atomic shell is about $2'$ (or 2.4 pc at a distance of 4.1 kpc, see Gas Shell-a in Figure 2). If the SNR encounters the molecular shell, the shock is significantly decelerated by the interaction with the dense gas. MCs are known to be clumpy (e.g., a volume filling factor of < 0.1 for dense clumps, [Blitz 1993](#)). That is, the SNR shock evolves mainly in the interclump medium (e.g., $n_{\text{H}} \sim 10 \text{ H atoms cm}^{-3}$). Therefore, the shock in the interclump medium and the surrounding ISM with lower density may be still moving while the shock in dense molecular clumps nearly stalls out. The dynamic time of the moving atomic gas thus can be estimated as $\Delta R/v_{\text{exp}} \sim 2.4 \text{ pc}/40 \text{ km s}^{-1} = 0.6 \times 10^5 \text{ years}$. The dynamic timescale of the moving atomic shell is slightly smaller and comparable with the remnant's age of $\gtrsim 0.7 \times 10^5 \text{ years}$ (see below). On the other hand, both of the atomic and the molecular shells seem to almost overlap at the outer region (or the northwestern region, see Gas Shell-b in Figure 2), suggesting the recent interaction between the shock and the dense gas at the boundary of the remnant.

One might wonder whether the shocked molecular gas, as well as the associated high-velocity HI shells, is related to other energetic sources, such as nearby HII regions and/or the stellar winds from massive OB stars. However, these possibilities can be excluded because of lacking the associated energetic sources in the direction. Some HII regions with small sizes of $\lesssim 2'$ (e.g., [Anderson et al. 2011, 2014](#)) are distributed in the FOV, but they are at least $\sim 6'$ (7 pc at a distance of 4.1 kpc) away from identified shocked BML regions. Actually, the overlapping case between HII regions and BML regions can be exactly picked out because HII regions have bright IR and non-thermal radio emission (see the two blue circles in Figures 4 and 6). A young massive cluster of Mercer 20 located at ($l=44^\circ 16'$, $b=-0^\circ 07'$) contains several massive stars within a radius of $\sim 1'$ ([Mercer et al. 2005](#); [Messineo et al. 2009](#)). Although these OB stars at a distance of $\sim 3.8 \text{ kpc}$ ([Messineo et al. 2009](#)) or $\sim 8.2 \text{ kpc}$ ([de la Fuente et al. 2015](#)) are projected on the northeastern border of the high-velocity HI shells, they are unlikely responsible for the large-scale neutral atomic shells with sizes of ~ 0.4 (or 28.6 pc at 4.1 kpc) and the widely distributed BML regions.

We thus suggest that an old SNR at a distance of 4.1 kpc (see below) appears to be a promising candidate for the surrounding shocked molecular gas and the high-velocity neutral atomic shells, although no corresponding radio feature has been detected in the VGPS 1.4 GHz continuum emission.

The missing radio structure is probably due to the faint synchrotron emission of the old SNR (see Section 3.4), the sensitivity limitation of the radio observation, the contamination of the diffuse radio emission in the Galactic plane, and the confusion of bright radio sources projected onto the area. Further high-resolution and sensitivity radio observations toward the region should be carried out to investigate the possible non-thermal radio emission.

In subsequent analysis, we investigate properties of the likely SNR. First, the distance is one of the most important values for studying the nature of the source. Spectroscopic information of the quiescent molecular gas is thus helpful for identifying the LSR velocity of MCs and associating its kinematic distance to the target that we are interested in. For the $V_{\text{LSR}} = +60 \text{ km s}^{-1}$ molecular gas, we find that most of ^{13}CO peaks from the shocked gas and the molecular shells correspond to H I dips, indicating that they are likely at near distance based on the H I self-absorption method (Roman-Duval et al. 2009). Accordingly, we adopt a near distance as the distance of the $+60 \text{ km s}^{-1}$ GMC and exclude the far distance. Using the A5 rotation curve model of Reid et al. (2014), we place the $+60 \text{ km s}^{-1}$ GMC and the associated SNR at a near kinematic distance of 4.1 kpc.

Second, as the brightness temperature of the H I shells is relatively low ($\sim 1 \text{ K}$ at $+100 \text{ km s}^{-1}$), we may assume that the high-velocity atomic gas is optically thin. Then the H I mass of the high-velocity shells is estimated to be $\gtrsim 230d_{4.1}^2 M_{\odot}$, where $d_{4.1}$ is the distance to the cloud in units of 4.1 kpc. Adopting a radius of $0^{\circ}405$ (e.g., $(0^{\circ}49+0^{\circ}32)/2$, Gottschall et al. 2016), the solid angle of the high-velocity H I shells is about 0.24 sr. The derived total H I mass for a sphere with a radius of $0^{\circ}405$ is $\gtrsim 1.2d_{4.1}^2 \times 10^4 M_{\odot}$, which corresponds to a kinetic energy of $\gtrsim 1.9d_{4.1}^2 \times 10^{50}$ ergs for the expansion velocity of $v_{\text{exp}} \gtrsim 40 \text{ km s}^{-1}$. A small fraction of 10% energy from a single supernova explosion with a total mechanical energy of 1.9×10^{51} erg is sufficient to power the expanding atomic gas, favoring an SNR origin for the disturbed gas that is widely distributed in the FOV.

Third, the pre-explosion ambient density is estimated to be $\sim 3.7d_{4.1}^{-1} \text{ cm}^{-3}$ if the neutral gas with total mass of $1.2d_{4.1}^2 \times 10^4 M_{\odot}$ was uniformly distributed within a sphere of a radius of 29.0 pc ($0^{\circ}405$ at a distance of 4.1 kpc). According to Cioffi et al. (1988) for an SNR in the pressure-driven snowplow phase, the explosion energy could be: $E_{\text{SN}} = 6.8 \times 10^{43} n_0^{1.16} v_{\text{exp}}^{1.35} R_s^{3.16} \zeta_m^{0.161} \text{ erg} \sim 1.9d_{4.1}^2 \times 10^{51} \text{ erg}$, where $n_0 = 3.7d_{4.1}^{-1} \text{ cm}^{-3}$, $v_{\text{exp}} = 40 \text{ km s}^{-1}$, $R_s = 29.0d_{4.1} \text{ pc}$, and $\zeta_m = Z/Z_{\odot} = 1$. The estimated explosion energy of $1.9d_{4.1}^2 \times 10^{51} \text{ erg}$ is slightly larger than the typical value of 1×10^{51} ergs, but still reasonable. If the material inside the volume is not uniformly distributed, the above total mass of $1.2d_{4.1}^2 \times 10^4 M_{\odot}$ is probably overestimated, leading to the larger explosion energy for an SNR. It is a more realistic case because the neutral atomic shells with the highest velocity of $97.5\text{--}111.5 \text{ km s}^{-1}$ are only detected near the western boundary of HESS J1912+101.

The age of the SNR could be $2R_s/(7v_{\text{exp}}) \lesssim 2.0 \times 10^5$ years for a radius of 29.0 pc and an expansion velocity of $v_{\text{exp}} \gtrsim 40 \text{ km s}^{-1}$ in the radiative pressure-driven snowplow phase. We stress that the above value is an upper limit due to the somewhat underestimated velocity of the remnant's shock. Some atomic gas structures with higher velocity but lower intensity may be lost because of confusion from the diffuse emission of the Galactic plane. Additionally, the evolutionary phase of the remnant should be speeded up if the SNR evolves in the environment of a pre-existent wind bubble (e.g., Dwarkadas 2005, 2007).

The lower limit of the SNR age may be obtained from the view of radiative cooling of the remnant. According to little X-ray emission and the low shock velocity of $\sim 40 \text{ km s}^{-1}$ in our case, we suggest that the SNR has lost a substantial amount of explosion energy from radiative cool-

ing. The forward shock of the remnant is also significantly decelerated. The SNR age is thus at least 2–3 times larger than the transition time, which is defined as the time of an adiabatic Sedov–Taylor blast wave to a radiative pressure-driven snowplow phase. The transition time is given by $t_{\text{tr}} \approx 2.9 \times 10^4 (\frac{E_{\text{SN}}}{10^{51} \text{ erg}})^{4/17} (\frac{n}{1 \text{ cm}^{-3}})^{-9/17}$ years (e.g., Blondin et al. 1998). Assuming $n \sim 1 \text{ cm}^{-3}$, $E_{\text{SN}} \sim 1 \times 10^{51} \text{ erg}$, and $t_{\text{SNR}} \gtrsim 3 \times t_{\text{tr}}$, the SNR age is $\gtrsim 0.9 \times 10^5$ years, which is reasonably consistent with numerical simulations of $\gtrsim (0.7\text{--}1.1) \times 10^5$ years that the SNR has radiated most of its explosion energy in the wind-bubble environment (e.g., Figures 3 and 8 in Tenorio-Tagle et al. 1991). The age of the SNR is thus $(0.7\text{--}2.0) \times 10^5$ years.

We also note that two pulsars, PSR J1913+1000 and PSR J1913+1011, are situated within the inner shell of HESS J1912+101. PSR J1913+1000 (Hobbs et al. 2004) is not related to the old SNR because of their different distances ($d_{\text{PSR}} \sim 7.9 \text{ kpc}$ vs. $d_{\text{SNR}} \sim 4.1 \text{ kpc}$) and ages ($t_{\text{PSR}} \sim 7.9 \times 10^5$ years vs. $t_{\text{SNR}} \sim (0.7\text{--}2.0) \times 10^5$ years). Meanwhile, PSR J1913+1011, which is located at ($l=44^\circ 48'$, $b=-0^\circ 17'$) and is close to the geometric center of HESS J1912+101 (see Figure 1), has a distance of 4.5 kpc from dispersion measurements and an age of 1.7×10^5 years from the spin-down method. Both of the two values are consistent well with the estimated distance and age of the remnant, indicating that PSR J1913+1011 is probably the result of the core collapse of the massive progenitor of the old SNR.

The progenitor’s wind of the old SNR may excavate its surrounding and form a pre-existing wind-blown bubble before the supernova explosion. Assuming that the remnant’s progenitor was a massive single star and the current molecular shells are mainly generated by its massive wind, we can estimate its mass from the cavity size. The size of the $+60 \text{ km s}^{-1}$ GMC is comparable to the TeV shell’s size of HESS J1912+101 (Figures 1 and 4). Adopting the inner radius of 22.9 pc ($0^\circ 32'$) as the radius of the wind bubble, an initial stellar mass of $\gtrsim 26 M_\odot$ is obtained from the linear relation between the progenitor’s mass and the wind bubble’s radius (see Equation 8 and Figure 1 in Chen et al. 2013). It implies that the progenitor’s spectral type is probably earlier than O9V in a constant interclump pressure of $p/k \sim 10^5 \text{ cm}^{-3} \text{ K}$.

Briefly, an old SNR seems to be the origin of the shocked molecular gas and high-velocity H I shells. In this case, the mass of the ambient gas is swept up by the wind of the massive progenitor of the SNR and the gas in the formed shell is accelerated by the SNR’s shock. The kinetic energy of the disturbed gas is also provided by the remnant, resulting in the remarkable morphological and kinematic features of the molecular and atomic gas shown by us (Figure 2). The non-detection in the X-ray bands, together with the absence of corresponding radio structures in the surrounding, is consistent with the SNR’s old age of $(0.7\text{--}2.0) \times 10^5$ years (see Section 3.4).

3.4. Origin of the shell-like TeV source of HESS J1912+101

The PWN and the SNR scenarios for HESS J1912+101 were discussed recently (Aharonian et al. 2008b; Puehlhofer et al. 2015). However, the origin of the TeV source is yet unconfirmed. It is worth mentioning that TeV sources of ARGO J1912+1026 (centered at $l=44^\circ 59'$ and $b=0^\circ 20'$, the angular resolution $\sim 0^\circ 17'\text{--}1^\circ 66'$, Bartoli et al. 2013) and 2HWC J1912+099 (centered at $l=44^\circ 15'$ and $b=-0^\circ 08'$, the angular resolution $\sim 0^\circ 2'\text{--}1^\circ 0'$, Abeysekara et al. 2017) were proposed to be associated with HESS J1912+101. All of these characteristics indicate that the high-energy TeV emission is significantly enhanced in such a region. In our opinion, the high-energy γ -ray emission in the region can be explained by interactions between accelerated particles from the SNR and the surrounding dense medium.

We have revealed that shocked MCs, together with the associated high-velocity atomic gas, are concentrated toward HESS J1912+101. Especially, the shocked MCs with broadline wings, as well as the expanding H I shells (Figure 2), are observed mainly projected close to the western boundary of the TeV source. These interesting features indicate large amounts of momentum and mechanical energy injection to the disturbed gas. We suggest that an energetic source is initially required at the southeast region of the gas shells to account for the kinematic features of the disturbed gas on a large scale. An old SNR may be a good choice and a reasonable candidate because of lacking other energetic sources, e.g., giant H II regions or massive OB stars (see Section 3.3). As a consequence, the SNR would provide the required energy of the high-energy protons.

The angular resolution of H.E.S.S. observation is better than $0^\circ.1$, which allows us to compare the TeV emission with the distribution of the shocked and/or dense molecular gas with the precision of several arcmin. The distribution of the high-energy emission of HESS J1912+101 is not uniform. Several enhanced TeV peaks ($\gtrsim 5\sigma$) can be seen at ($l \sim 44^\circ.3$, $b \sim 0^\circ.1$), ($l \sim 44^\circ.2$, $b \sim -0^\circ.3$), ($l \sim 44^\circ.6$, $b \sim -0^\circ.4$), ($l \sim 44^\circ.8$, $b \sim -0^\circ.3$), and ($l \sim 44^\circ.7$, $b \sim 0^\circ.0$). Based on CO data, we find that the shocked gas and/or dense MCs are spatially coincident with the VHE γ -ray emission.

The size of the 60 km s^{-1} MC concentration is comparable to that of the TeV source of HESS J1912+101 (Figures 1 and 4). Generally, the overall ^{13}CO emission is strong in the western part of the TeV shell, which is consistent with the brighter high-energy emission on the western half of HESS J1912+101. TeV source 2HWC J1912+099 (Abeysekara et al. 2017) appears projected onto such the region, in which the disturbed ISM is also concentrated (see Figure 2). The BML regions (e.g., SCa, SCb, SCd, SCe, and SC1–SC4) show good spatial coincidences with the TeV enhancement (Figure 4). At ($l \sim 44^\circ.3$, $b \sim 0^\circ.1$), the dense (traced by ^{13}CO emission, $\sim 10^2$ – 10^3 cm^{-3}) and massive ($\sim 3 \times 10^4 M_\odot$) MC complex at $\sim +60 \text{ km s}^{-1}$, which is related to an IR bubble N91 (Churchwell et al. 2006) at a massive star-forming region (e.g., Gong et al. 2017 (to be submitted) and Dirienzo et al. 2012), is spatially coincident with the brightest TeV emission there. On the contrary, the eastern ^{13}CO emission is relatively weak. However, a piece of ^{13}CO cloud (size $\sim 3'$ and $V_{\text{LSR}} \sim +58 \text{ km s}^{-1}$), together with more extended ^{12}CO emission, is located at ($l \sim 44^\circ.72$, $b \sim 0^\circ.03$). Some patches of molecular gas with weak ^{13}CO emission also can be seen along the eastern inner shell of the TeV source (Figures 1 and 4), which may be related to the relatively weak γ -ray emission on the eastern half of HESS J1912+101.

The detection of the H I and CO partial shell-like structures, as well as the C^{18}O emission in some regions, shows that the old SNR is located in the complex and dense ISM. Naturally, the established source-target (or SNR–MCs) system favors the hadronic scenario for the observed TeV emission (e.g., Yamazaki et al. 2006; Gabici et al. 2009). The hadronic γ -ray flux can be estimated by Drury et al. (1994) as $F_\gamma(> 0.681 \text{ TeV}) \approx 9 \times 10^{-11} \Theta (E/1 \text{ TeV})^{-1.1} (E_{\text{SN}}/10^{51} \text{ erg}) (d/1 \text{ kpc})^{-2} (n/1 \text{ cm}^{-3})$. Here, Θ is the fraction of the total supernova explosion energy converted to CR. Using numerical values of $F_\gamma(> 0.681 \text{ TeV}) = 4.5 \times 10^{-12} \text{ photons cm}^{-2} \text{ s}^{-1}$, $\Theta = 0.1$ – 0.01 , $E_{\text{SN}} = 10^{51} \text{ erg}$, and $d = 4.1 \text{ kpc}$, the hadronic scenario requires a mean target gas density of 6–60 cm^{-3} for the surrounding ISM, which is consistent with our finding of the molecular environment there.

According to the spectral fit of HESS J1912+101 (Gottschall et al. 2016), the energy flux in the 1–10 TeV band is estimated to be $F(1 - 10 \text{ TeV}) = 8.1 \times 10^{-12} \text{ erg cm}^{-2} \text{ s}^{-1}$. Using *Chandra* data, Chang et al. (2008) found that the upper limit of the X-ray flux in the 0.3–10 keV band is $0.7 \times 10^{-13} \text{ erg cm}^{-2} \text{ s}^{-1}$ for the center of gravity of HESS J1912+101. It indicates that the flux ratio

of $R_{\text{TeV}(1-10 \text{ TeV})/\text{X-ray}(0.3-10 \text{ keV})}$ should be larger than 120. The high flux ratio agrees with the case of interactions between an old SNR and its ambient GMC (e.g., Yamazaki et al. 2006).

In the scenario, the GeV emission from the system may be dim with respect to the TeV emission as shown in Table 2 of Yamazaki et al. (2006). If the contribution of CR protons for the GeV band emission can be neglected, the total energy of the accelerated protons for the 1–10 TeV emission is estimated to be $W_p^{\text{total}}(10-100 \text{ TeV}) \approx L_\gamma(1-10 \text{ TeV})\tau_{\text{pp}}$, where, $L_\gamma(1-10 \text{ TeV})=4\pi d^2 F(1-10 \text{ TeV}) \approx 1.6 \times 10^{34} (d/4.1 \text{ kpc})^2 \text{ erg s}^{-1}$ is the luminosity of the source in the 1–10 TeV band. Adopting the characteristic cooling time of inelastic pp-interactions of $\tau_{\text{pp}}=4.4 \times 10^{15} (n_{\text{gas}}/1 \text{ cm}^{-3})^{-1} \text{ s}$ (Aharonian 2004) and a mean medium density of 60 cm^{-3} for the molecular environment, $W_p^{\text{total}}(10-100 \text{ TeV}) \approx 1.2 \times 10^{48} (d/4.1 \text{ kpc})^2 (n_{\text{gas}}/60 \text{ cm}^{-3})^{-1} \text{ erg}$. Therefore, an SNR's mechanical explosion energy of 10^{51} erg may be sufficient enough to explain the observed TeV flux by pp-interactions in a distance of 4.1 kpc and an average density of $\sim 10^2 \text{ cm}^{-3}$.

Finally, adopting $R_{\text{TeV}(1-10 \text{ TeV})/\text{radio}(10^7-10^{11} \text{ Hz})}=350-50$ (Yamazaki et al. 2006) and a non-thermal radio spectral index of $\alpha=-0.5$ for an SNR (e.g., a power-law spectrum of $S(\nu) \propto \nu^\alpha$), an integral flux from 10^7 to 10^{11} Hz of $F_{\text{radio}}=2.3 \times 10^{-14}-1.6 \times 10^{-13} \text{ erg cm}^{-2} \text{ s}^{-1}$ corresponds to a flux density of 0.1–0.7 Jy at 1.4 GHz. Such a low radio flux density indicates that the remnant's feature is difficult to be discerned from the diffuse background emission of the Galactic plane based on the current radio survey (e.g., see Figure 10 in Anderson et al. 2017).

4. SUMMARY AND CONCLUSIONS

We have studied the CO and H I data toward the shell-like TeV source of HESS J1912+101. The main results and conclusions are summarized as follows.

1. Both of the shocked molecular gas and the high-velocity H I atomic gas are found to be toward the shell-like TeV source of HESS J1912+101. The velocity of the ^{12}CO broadening is obviously up to $V_{\text{LSR}} \sim +80 \text{ km s}^{-1}$ with respect to the unperturbed dense molecular gas at $V_{\text{LSR}} \sim +60 \text{ km s}^{-1}$ traced by ^{13}CO and C^{18}O ($J=1-0$) emission.

2. The disturbed molecular gas shows compelling signs of the redshifted-broadening ($\gtrsim 20 \text{ km s}^{-1}$) in ^{12}CO ($J=1-0$) and ^{12}CO ($J=3-2$) lines, which is consistent with the discovery of the high-velocity atomic shells up to $V_{\text{LSR}} \gtrsim +100 \text{ km s}^{-1}$ at the same region. The high-velocity H I shells are indeed found to be coincident with the molecular partial shells, suggesting the physical association between them.

3. The shocked molecular gas, the quiescent molecular gas, and the high-velocity atomic gas seem to be arranged orderly from southeast to northwest, indicating an energetic source with large momentum and mechanical energy injection in the southeastern region of the disturbed gas concentration. After excluding other energetic sources such as H II regions and massive OB stars, we suggest that an old SNR is probably responsible for the origin of the disturbed gas.

4. We place the old SNR at a near kinematic distance of 4.1 kpc based on the association between the remnant and the $+60 \text{ km s}^{-1}$ MCs. The far kinematic distance of the source can be excluded because most of the ^{13}CO emission from the shocked gas and the molecular shells has corresponding H I dips at $\sim +60 \text{ km s}^{-1}$. The age of the remnant is estimated to be $\sim (0.7-2.0) \times 10^5$ years according to the evolution of the SNR in a pre-existent wind bubble from the massive progenitor star.

5. PSR J1913+1011, which seems to be just located near the centroid of HESS J1912+101, probably results from the core collapse of the massive progenitor of the old SNR because of their comparable ages ($t_{\text{PSR}} \sim 1.7 \times 10^5$ years vs. $t_{\text{SNR}} \sim (0.7-2.0) \times 10^5$ years) and distances ($d_{\text{PSR}} \sim 4.5 \text{ kpc}$ vs.

$d_{\text{SNR}} \sim 4.1$ kpc). The massive progenitor of the remnant blew or carved a molecular bubble via its energetic stellar winds, which has a comparable size with the TeV shell or the $+60 \text{ km s}^{-1}$ GMC. Accordingly, the spectral type of its main-sequence star is probably earlier than O9V assuming that a massive single star evolved in a constant interclump pressure of $p/k \sim 10^5 \text{ cm}^{-3} \text{ K}$.

6. We suggest that the old SNR may be a promising candidate for the shell-like TeV source HESS J1912+101, although no corresponding radio and X-ray counterpart has been detected. The SNR's old age of $\sim (0.7-2.0) \times 10^5$ years could be responsible for the absence of its radio and X-ray emission. In the scenario, the shell-like high-energy emission comes from the decay of neutral pions produced by interactions of accelerated hadrons from the SNR's shock and the surrounding dense gas.

7. Further high-resolution and sensitivity radio observations toward the TeV source should be carried out to investigate the possible non-thermal radio emission of the old SNR.

The authors acknowledge the staff members of the Qinghai Radio Observing Station at Delingha for their support of the observations. We thank the anonymous referee for valuable comments and suggestions that helped to improve this paper. This work is supported in part by National Key R&D Program of China (2017YFA0402700). Y.S. acknowledges support from NSFC grants 11233001 and 11233007. X.Z. acknowledges support from NSFC grant 11403104 and Jiangsu Provincial Natural Science Foundation grant BK20141044. Y.C. acknowledges support from 973 Program grant 2015CB857100 and NSFC grant 11633007. Y.G. acknowledges support from NSFC grant 11127903.

Facility: PMO 13.7m

Software: GILDAS/CLASS (Pety 2005)

REFERENCES

- Abeysekara, A. U., Albert, A., Alfaro, R., et al. 2017, *ApJ*, 843, 40
- Ackermann, M., Ajello, M., Allafort, A., et al. 2013, *Science*, 339, 807
- Aharonian, F., Akhperjanian, A. G., Bazer-Bachi, A. R., et al. 2008a, *A&A*, 481, 401
- Aharonian, F., Akhperjanian, A. G., Barres de Almeida, U., et al. 2008b, *A&A*, 484, 435
- Aharonian, F. A. 2004, Very high energy cosmic gamma radiation : a crucial window on the extreme Universe (World Scientific Publishing Co), doi:10.1142/4657
- Anderson, L. D., Bania, T. M., Balser, D. S., et al. 2014, *ApJS*, 212, 1
- Anderson, L. D., Bania, T. M., Balser, D. S., & Rood, R. T. 2011, *ApJS*, 194, 32
- Anderson, L. D., Wang, Y., Bihr, S., et al. 2017, *ArXiv e-prints*, arXiv:1705.10927
- Bartoli, B., Bernardini, P., Bi, X. J., et al. 2013, *ApJ*, 779, 27
- Blitz, L. 1993, in *Protostars and Planets III*, ed. E. H. Levy & J. I. Lunine, 125–161
- Blondin, J. M., Wright, E. B., Borkowski, K. J., & Reynolds, S. P. 1998, *ApJ*, 500, 342
- Bolatto, A. D., Wolfire, M., & Leroy, A. K. 2013, *ARA&A*, 51, 207
- Castets, A., & Langer, W. D. 1995, *A&A*, 294, 835
- Castro, D., & Slane, P. 2010, *ApJ*, 717, 372
- Chang, C., Konopelko, A., & Cui, W. 2008, *ApJ*, 682, 1177
- Chen, Y., Jiang, B., Zhou, P., et al. 2014, in *IAU Symposium*, Vol. 296, *Supernova Environmental Impacts*, ed. A. Ray & R. A. McCray, 170–177
- Chen, Y., Zhou, P., & Chu, Y.-H. 2013, *ApJL*, 769, L16
- Churchwell, E., Povich, M. S., Allen, D., et al. 2006, *ApJ*, 649, 759
- Cioffi, D. F., McKee, C. F., & Bertschinger, E. 1988, *ApJ*, 334, 252
- de la Fuente, D., Najarro, F., Trombley, C., Davies, B., & Figer, D. F. 2015, *A&A*, 575, A10

- Dempsey, J. T., Thomas, H. S., & Currie, M. J. 2013, *ApJS*, 209, 8
- Dirienzo, W. J., Indebetouw, R., Brogan, C., et al. 2012, *AJ*, 144, 173
- Drury, L. O., Aharonian, F. A., & Voelk, H. J. 1994, *A&A*, 287, 959
- Dwarkadas, V. V. 2005, *ApJ*, 630, 892
- . 2007, *ApJ*, 667, 226
- Frail, D. A., & Mitchell, G. F. 1998, *ApJ*, 508, 690
- Frerking, M. A., Langer, W. D., & Wilson, R. W. 1982, *ApJ*, 262, 590
- Fujita, Y., Ohira, Y., Tanaka, S. J., & Takahara, F. 2009, *ApJL*, 707, L179
- Gabici, S., Aharonian, F. A., & Casanova, S. 2009, *MNRAS*, 396, 1629
- Gottschall, D., Capasso, M., Deil, C., et al. 2016, *ArXiv e-prints*, arXiv:1612.00261
- Hobbs, G., Faulkner, A., Stairs, I. H., et al. 2004, *MNRAS*, 352, 1439
- Jiang, B., Chen, Y., Wang, J., et al. 2010, *ApJ*, 712, 1147
- Kilpatrick, C. D., Bieging, J. H., & Rieke, G. H. 2016, *ApJ*, 816, 1
- Koo, B.-C., & Heiles, C. 1991, *ApJ*, 382, 204
- Koo, B.-C., Kang, J.-H., & McClure-Griffiths, N. M. 2004, *Journal of Korean Astronomical Society*, 37, 61
- Li, H., & Chen, Y. 2010, *MNRAS*, 409, L35
- Mercer, E. P., Clemens, D. P., Meade, M. R., et al. 2005, *ApJ*, 635, 560
- Messineo, M., Davies, B., Ivanov, V. D., et al. 2009, *ApJ*, 697, 701
- Morris, D. J., Hobbs, G., Lyne, A. G., et al. 2002, *MNRAS*, 335, 275
- Ohira, Y., Murase, K., & Yamazaki, R. 2011, *MNRAS*, 410, 1577
- Park, G., Koo, B.-C., Gibson, S. J., et al. 2013, *ApJ*, 777, 14
- Pety, J. 2005, in *SF2A-2005: Semaine de l'Astrophysique Francaise*, ed. F. Casoli, T. Contini, J. M. Hameury, & L. Pagani, 721
- Puehlhofer, G., Brun, F., Capasso, M., et al. 2015, in *International Cosmic Ray Conference*, Vol. 34, 34th International Cosmic Ray Conference (ICRC2015), ed. A. S. Borisov, V. G. Denisova, Z. M. Guseva, E. A. Kanevskaya, M. G. Kogan, A. E. Morozov, V. S. Puchkov, S. E. Pyatovsky, G. P. Shoziyoev, M. D. Smirnova, A. V. Vargasov, V. I. Galkin, S. I. Nazarov, & R. A. Mukhamedshin, 886
- Reach, W. T., Rho, J., & Jarrett, T. H. 2005, *ApJ*, 618, 297
- Reid, M. J., Menten, K. M., Brunthaler, A., et al. 2014, *ApJ*, 783, 130
- Reynolds, S. P. 2008, *ARA&A*, 46, 89
- Roman-Duval, J., Jackson, J. M., Heyer, M., et al. 2009, *ApJ*, 699, 1153
- Seta, M., Hasegawa, T., Dame, T. M., et al. 1998, *ApJ*, 505, 286
- Shan, W. L., Yang, J., Shi, S. C., et al. 2012, *IEEE Transactions on Terahertz Science and Technology*, 2, 593
- Slane, P., Bykov, A., Ellison, D. C., Dubner, G., & Castro, D. 2015, *SSRv*, 188, 187
- Stil, J. M., Taylor, A. R., Dickey, J. M., et al. 2006, *AJ*, 132, 1158
- Su, Y., Sun, Y., Li, C., et al. 2016, *ApJ*, 828, 59
- Su, Y., Zhou, X., Yang, J., et al. 2017, *ApJ*, 836, 211
- Tavani, M., Giuliani, A., Chen, A. W., et al. 2010, *ApJL*, 710, L151
- Tenorio-Tagle, G., Rozyczka, M., Franco, J., & Bodenheimer, P. 1991, *MNRAS*, 251, 318
- Tian, W. W., Leahy, D. A., Haverkorn, M., & Jiang, B. 2008, *ApJL*, 679, L85
- Urquhart, J. S., Hoare, M. G., Purcell, C. R., et al. 2009, *A&A*, 501, 539
- Yamazaki, R., Kohri, K., Bamba, A., et al. 2006, *MNRAS*, 371, 1975

Table 1. Details of the Survey Data Used in the Analysis

Name	Survey Range	Line/Continuum	Resolution	rms sensitivity	Reference
MWISP	$-10^\circ < l < 250^\circ, b < 5^\circ$	$^{12}\text{CO } (J=1-0)$	$50'', 0.2 \text{ km s}^{-1}$	$\sim 0.5 \text{ K}$	(1)
		$^{13}\text{CO } (J=1-0)$	$50'', 0.2 \text{ km s}^{-1}$	$\sim 0.3 \text{ K}$	
		$\text{C}^{18}\text{O } (J=1-0)$	$50'', 0.2 \text{ km s}^{-1}$	$\sim 0.3 \text{ K}$	
COHRS	$10^\circ 25' < l < 17^\circ 5', b < 0^\circ 5'$	$^{12}\text{CO } (J=3-2)$	$17'', 1 \text{ km s}^{-1}$	$\sim 1 \text{ K}$	(2)
	$17^\circ 25' < l < 50^\circ 25', b < 0^\circ 25'$				
VGPS	$50^\circ 25' < l < 55^\circ 25', b < 0^\circ 5'$	H I line	$1', 1.56 \text{ km s}^{-1}$	$\sim 2 \text{ K}$	(3)
	$18^\circ < l < 46^\circ, b < 1^\circ 3'$				
	$46^\circ < l < 59^\circ, b < 1^\circ 9'$				
	$59^\circ < l < 67^\circ, b < 2^\circ 3'$	21 cm continuum	$1'$	$\sim 0.3 \text{ K}$	

NOTE— (1) The $34^\circ 75' < l < 45^\circ 25'$ and $-5^\circ 25' < b < 5^\circ 25'$ region has been completely mapped (Su et al. 2016). Also see the information in <http://english.dlh.pmo.cas.cn/ic/>; (2) Dempsey et al. (2013); (3) Stil et al. (2006).

Table 2. Properties of the High-velocity H I Shells

Name	Size	v_{LSR}^a	v_{exp}^b	T_{mean}^c	Column Density ^d	$n_{\text{shell}}^{e,f}$	H I Mass ^f	E_{kin}^f
	(arcmin \times arcmin)	(km s^{-1})	(km s^{-1})	(K)	(10^{20} cm^{-2})	(cm^{-3})	(M_\odot)	($\times 10^{48} \text{ ergs}$)
Shell-a	3.3×20.4	60	40	0.9	0.7	$5.8d_{4.1}^{-1}$	$70d_{4.1}^2$	$1.1d_{4.1}^2$
Shell-b	4.7×24.6	61	40	1.2	0.9	$5.2d_{4.1}^{-1}$	$160d_{4.1}^2$	$2.6d_{4.1}^2$

^aThe LSR velocity of the quiescent gas from the ^{13}CO and/or C^{18}O emission.

^bThe expansion velocity from the difference between the mean velocity of the shocked gas and the velocity of the quiescent gas.

^cThe mean temperature of the H I shell at 100 km s^{-1} after subtracting the surrounding background of $\sim 0.5 \text{ K}$.

^dThe column density calculated from $1.822 \times 10^{18} \times T_{\text{mean}} \times v_{\text{exp}} \text{ cm}^{-2}$.

^eAssuming a depth of 3.3 and 4.7 arcmin (the mean width of the arc) for the H I Shell-a and the H I Shell-b, respectively.

^fParameter $d_{4.1}$ is the distance to the cloud in units of 4.1 kpc (see Section 3).

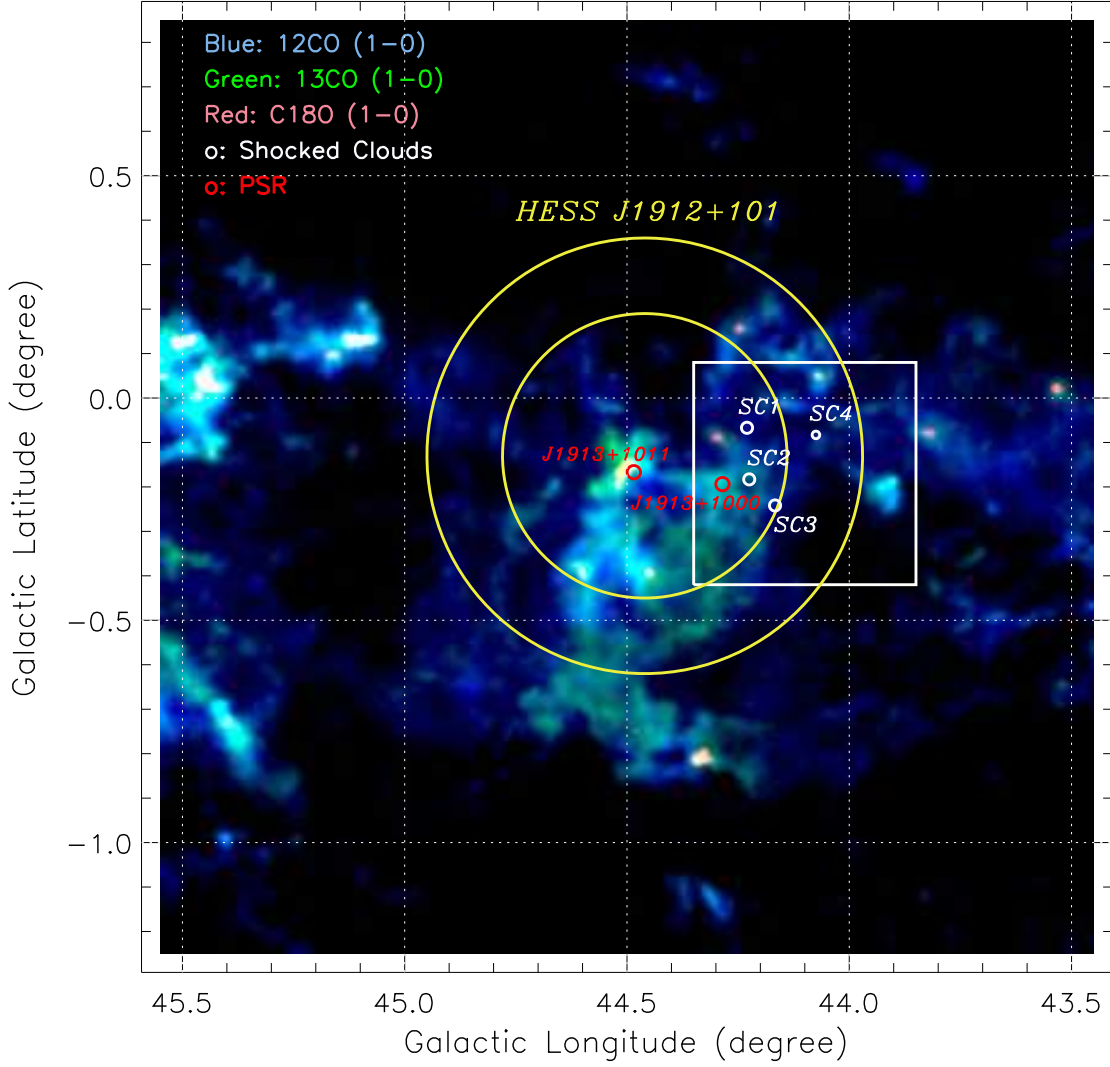


Figure 1. ^{12}CO ($J=1-0$, blue), ^{13}CO ($J=1-0$, green), and C^{18}O ($J=1-0$, red) intensity map toward HESS J1912+101 in the $58.5\text{--}62.0\text{ km s}^{-1}$ interval. The two yellow circles indicate the outer and inner TeV shells of HESS J1912+101 (Aharonian et al. 2008b; Gottschall et al. 2016), while the red and the white circles indicate the two pulsars (Morris et al. 2002; Hobbs et al. 2004) and the shocked clouds. The white box indicates the region shown in Figure 2.

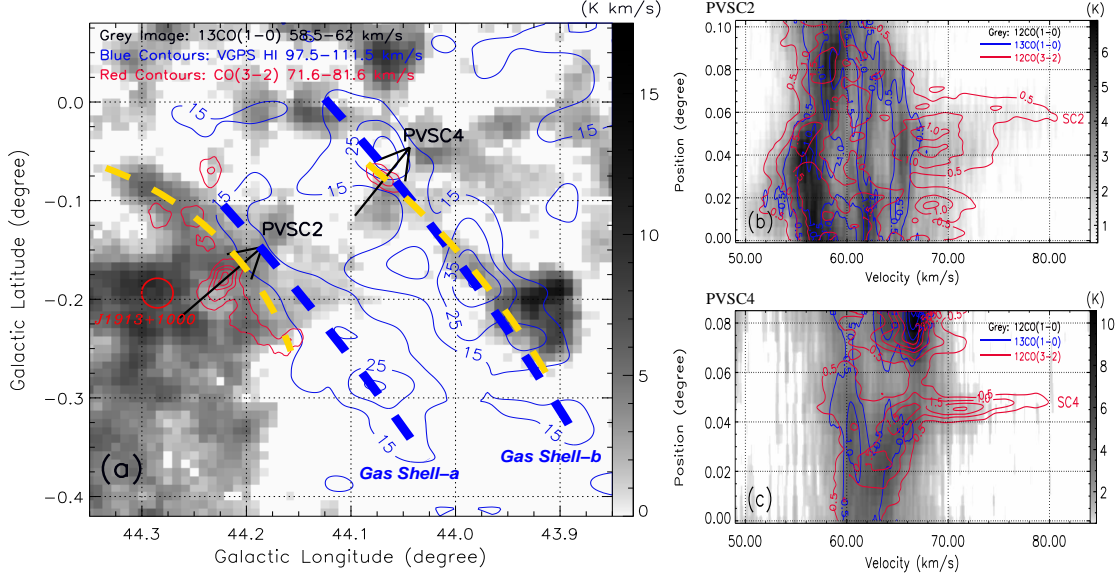


Figure 2. (a) ^{13}CO ($J=1-0$) emission in the interval of 58.5–62.0 km s^{-1} , overlaid with the high-velocity HI gas (blue, 97.5–111.5 km s^{-1}) and the shocked CO ($J=3-2$) gas (red, 71.6–81.6 km s^{-1}). The thick-dashed blue and gold lines represent the shells traced by the high-velocity HI gas and the unperturbed ^{13}CO gas, respectively. The two arrows, which just pass through the shocked BML regions of SC2 and SC4, indicate PV slices shown in panels (b) and (c), respectively. (b) PV diagram of ^{12}CO ($J=1-0$) emission along the arrow of PVSC2 overlaid with the blue contours of ^{13}CO emission and the red contours of CO ($J=3-2$) emission. The PV slice has a length of $6'.4$ (from $(l = 44^\circ 26', b = -0^\circ 21')$ to $(l = 44^\circ 18', b = -0^\circ 14')$) and a width of $1'.5$. (c) PV diagram of ^{12}CO ($J=1-0$) emission along the arrow of PVSC4. The PV slice has a length of $5'.2$ (from $(l = 44^\circ 09', b = -0^\circ 11')$ to $(l = 44^\circ 04', b = -0^\circ 04')$) and a width of $1'.5$.

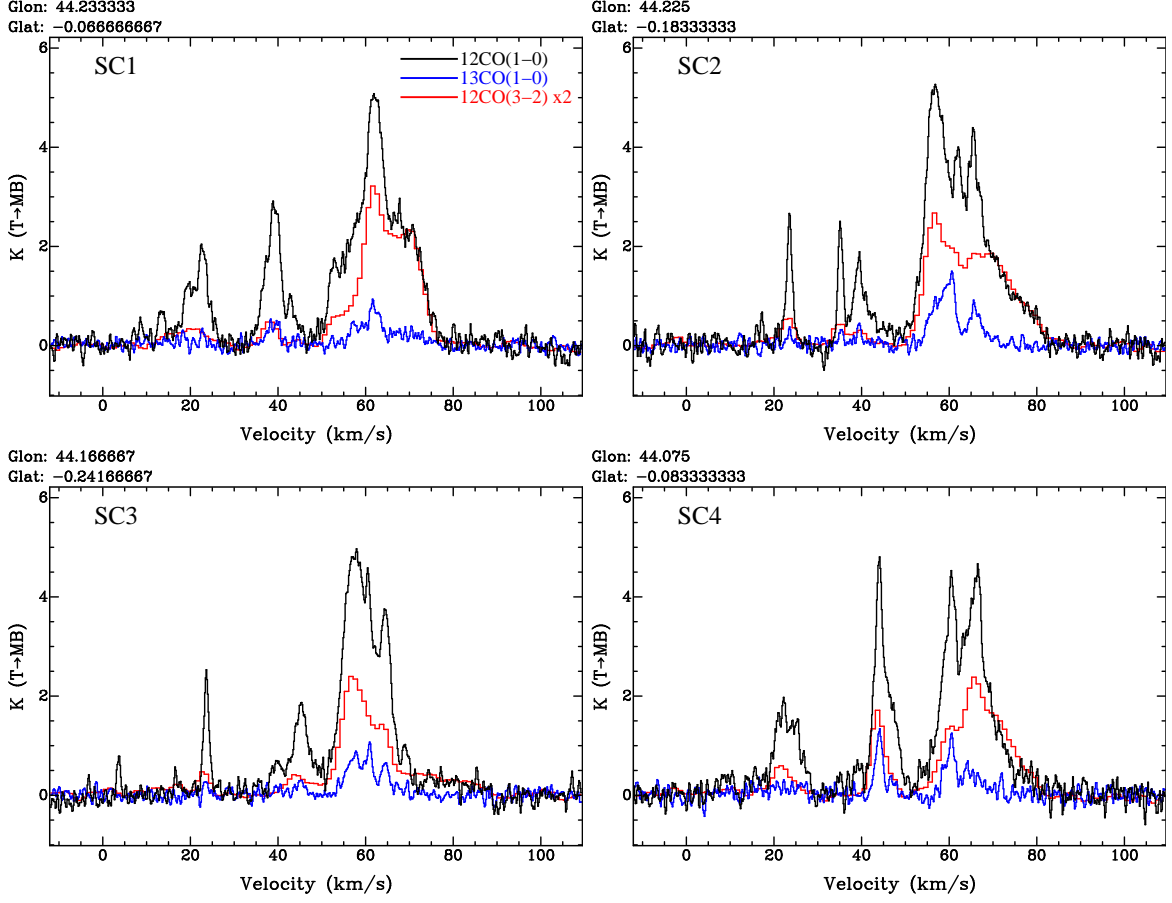


Figure 3. ^{12}CO ($J=1-0$; black), ^{13}CO ($J=1-0$; blue), and convolved ^{12}CO ($J=3-2$; red) spectra of shocked gas toward HESS J1912+101. Positions of shocked BML regions are labeled in Figure 1. These spectra are extracted from regions of $1'.5 \times 1'.5$, $1'.5 \times 1'.5$, $1'.5 \times 1'.5$, and $1'.0 \times 1'.0$ around points SC1–SC4, respectively.

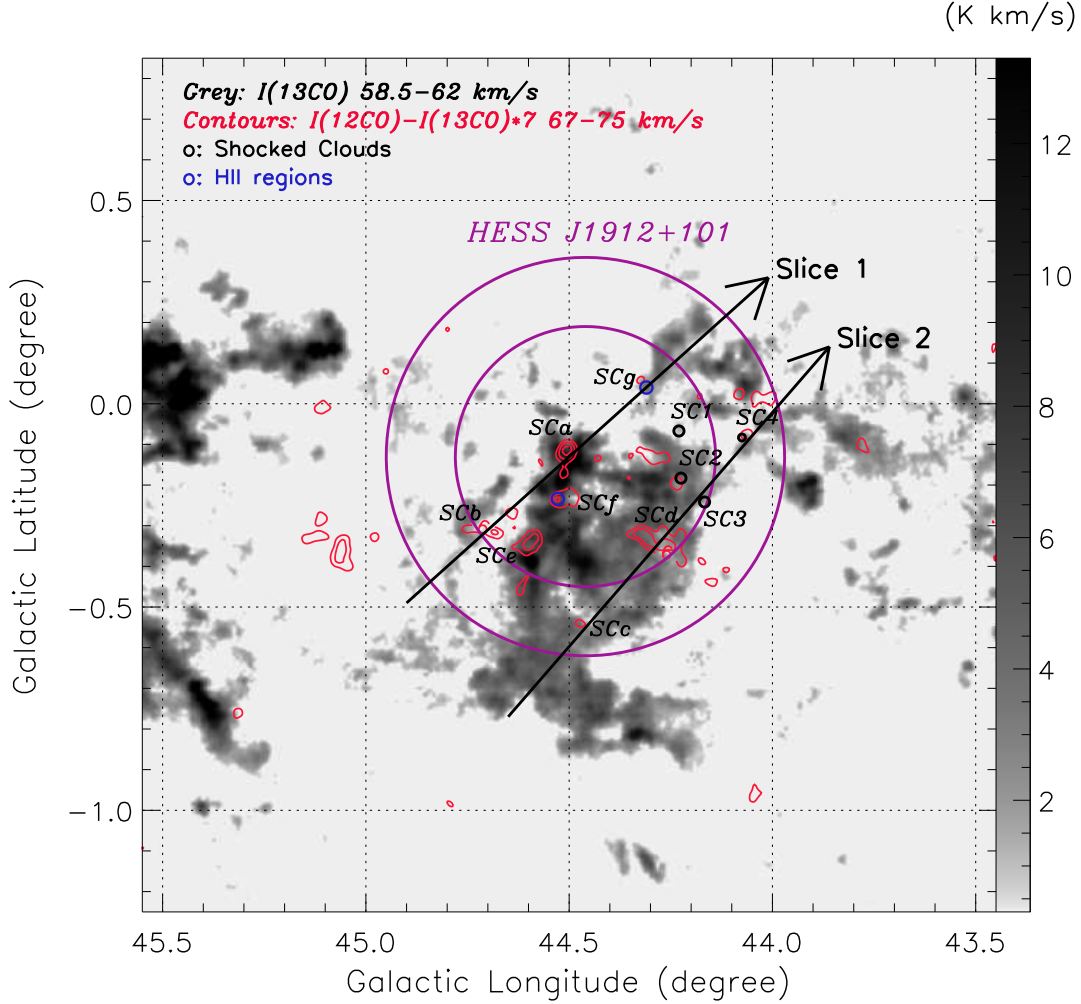


Figure 4. Integrated ^{13}CO ($J=1-0$) emission toward HESS J1912+101 in the interval of $58.5-62.0 \text{ km s}^{-1}$, overlaid with the red contours (6, 8, and 10 K km s^{-1}) of possible ^{12}CO ($J=1-0$) wing component in the interval of $67-75 \text{ km s}^{-1}$ (see text). The two purple circles indicate the outer and inner TeV shells of HESS J1912+101. The two arrows of Slice 1 and Slice 2 indicate PV slices shown in Figure 5. Positions and sizes of shocked BML regions of SC1–SC4 (see spectra in Figure 3) are also labeled. SCa–SCe indicate the possible shocked BML regions revealed from the ^{12}CO ($J=1-0$) wing component, while SCf and SCg may be contaminated by the nearby HII regions (the two blue circles for HRDS G044.528–0.234 and VLA G044.3103+00.0410; see the text).

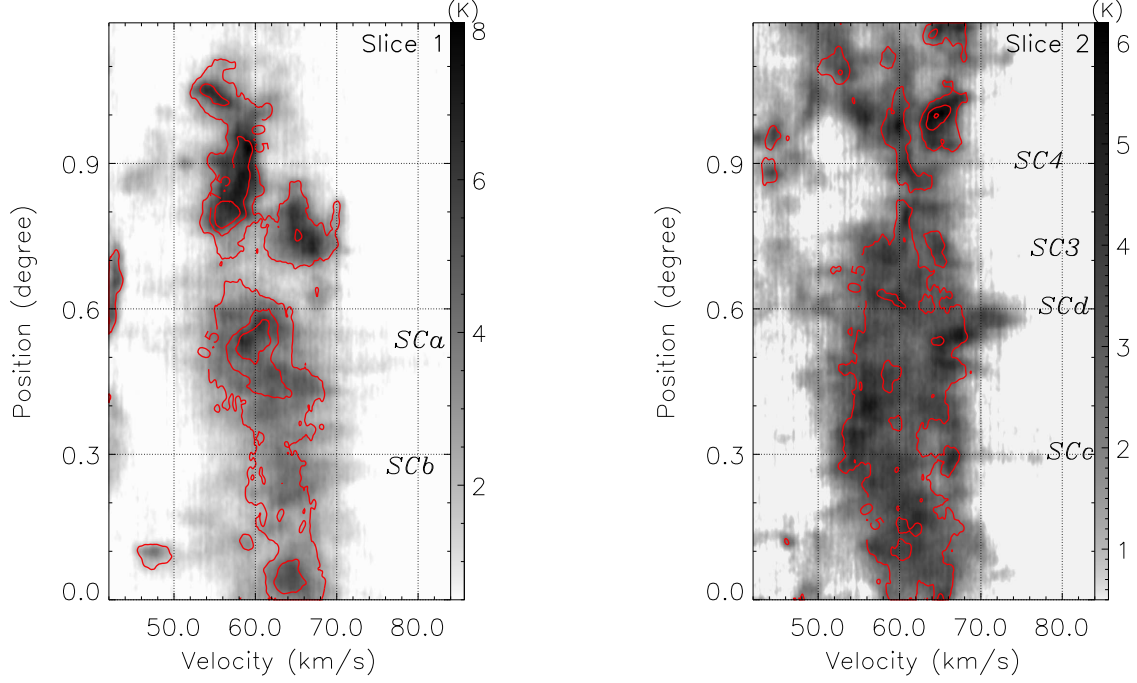


Figure 5. Left panel: PV diagram of ^{12}CO ($J=1-0$) emission along Slice 1, overlaid with the contours of ^{13}CO emission. The overlaid contour levels start from 0.5 K and increase by a step of 1 K. The PV slice has a length of $1^\circ.2$ (from $(l = 44^\circ.90, b = -0^\circ.49)$ to $(l = 44^\circ.01, b = 0^\circ.31)$) and a width of $5'.5$ (see the arrow Slice 1 in Figure 4). Right panel: PV diagram of ^{12}CO ($J=1-0$) emission along Slice 2, overlaid with the contours of ^{13}CO emission. The overlaid contour levels also start from 0.5 K and increase by a step of 1 K. The PV slice has a length of $1^\circ.2$ (from $(l = 44^\circ.65, b = -0^\circ.77)$ to $(l = 43^\circ.86, b = 0^\circ.14)$) and a width of $5'.5$ (see the arrow Slice 2 in Figure 4).

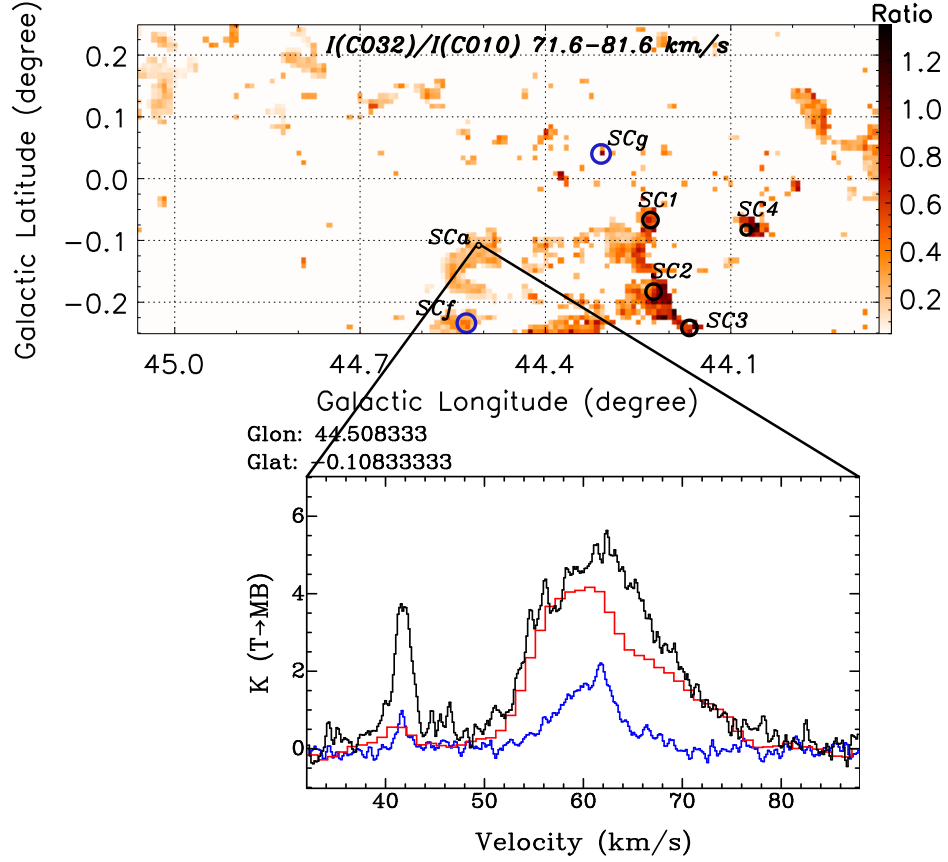


Figure 6. Map of the $^{12}\text{CO } J=3-2/1-0$ intensity ratio toward HESS J1912+101 at the velocity range of $71.6-81.6 \text{ km s}^{-1}$ after convolving the COHRS $^{12}\text{CO } (J=3-2)$ data to the same beam size as the MWISP $^{12}\text{CO } (J=1-0)$ data. The spectra of position $l=44^\circ 508$ and $b=-0^\circ 108$ with size of $0''.5$ in SCa are also given, where $^{12}\text{CO } (J=1-0)$, $^{13}\text{CO } (J=1-0)$, and $^{12}\text{CO } (J=3-2) \times 2$ are in black, blue, and red, respectively. Note that the unconvolved $^{12}\text{CO } (J=3-2)$ spectrum is shown to highlight the redshifted-broadening. The two blue circles show the H II regions of HRDS G044.528-0.234 and VLA G044.3103+00.0410.